Algorithm Theoretical Basis Document for the "Automatic Satellite Image Interpretation – Next Generation" Processor of the NWC/GEO

NWC/CDOP3/GEO/ZAMG/SCI/ATBD/ASII-NG, Issue 1.0.1

28 February 2022

Applicable to

GEO-ASII-NG NWC-088

which is comprised of

GEO-ASII-TF-v2.1

GEO-ASII-GW-v1.1

Prepared by ZAMG

REPORT SIGNATURE TABLE

Function	Name	Signature	Date
Prepared by	A. Jann, A. Wirth & B. Zeiner (ZAMG)		*28 February 2022*
Revised by	A. Wirth (ZAMG)		*28 February 2022*
Reviewed by	R. Goler, A. Jann (ZAMG)		*28 February 2022*
Authorised by	Pilar Rípodas SAFNWC Project Manager		*28 February 2022*

DOCUMENT CHANGE RECORD

Version	Date	Pages	CHANGE(S)
1.0.1	28 February *2022*	21	Version for SAFNWC/GEO v2021 (ASII-TF tuned to GOES-R and HIMAWARI input; algorithmic ASII-GW improvements of vMTG advanced to this release).

Table of contents

List of Tables and Figures

1. INTRODUCTION

1.1 Scope of the document

This document is the Algorithm Theoretical Basis Document for the "Automatic Satellite Image Interpretation – Next Generation" (ASII-NG) / PGE 17 of the NWC/GEO software package.

This document contains a description of the algorithms, including scientific aspects and practical considerations.

1.2 Software Version Identification

This document describes the algorithms implemented in the PGE 17 version included in the 2021 NWC/GEO software package delivery. The PGE has two sub-modules: the detection of tropopause foldings, ASII-TF v2.1, and the detection of gravity wave patterns, ASII-GW v1.1.

1.3 Improvements since the previous release

ASII-TF tuned for GOES-R and Himawari; enhanced gravity wave detection algorithm, IR analysis enabled for ASII-GW, and more comprehensive quality indicators introduced.

1.4 Definitions, Acronyms and Abbreviations

ASII	Automatic Satellite Image Interpretation
ASII-GW	Gravity wave detection sub-product of ASII-NG
ASII-NG	ASII next generation
ASII-TF	Tropopause folding detection sub-product of ASII-NG
BT	Brightness Temperature
CAT	clear air turbulence
HRV	High Resolution Visible
HRW	High Resolution Winds
IR	infrared
NWP	Numerical Weather Prediction
PIREP	Pilot Report
PVA	positive vorticity advection
RDT-CW	Rapidly Developing Thunderstorms – Convection Warning
REF	Reflectivity
SEVIRI	Spinning Enhanced Visible and Infra-Red Imager
VIS	Visible
WV	water vapour
ZAMG	Zentralanstalt für Meteorologie und Geodynamik

1.5 REFERENCES

1.5.1 Applicable Documents

The following documents, of the exact issue shown, form part of this document to the extent specified herein. Applicable documents are those referenced in the Contract or approved by the Approval Authority. They are referenced in this document in the form [AD.X]

For dated references, subsequent amendments to, or revisions of, any of these publications do not apply. For undated references, the current edition of the document referred applies.

Current documentation can be found at the NWC SAF Helpdesk web: http://www.nwc-saf.eumetsat.int

Ref	Title	Code	Vers	Date
[AD.1]	Project Plan for the NWCSAF CDOP3 phase	NWC/CDOP3/SAF/AEMET/MGT/PP	1.6	01/12/21
[AD.2]	NWCSAF CDOP3 Project Plan Master Schedule	NWC/CDOP3/SAF/AEMET/MGT/PP/MasterSchedule	1.6	01/12/21
[AD.3]	Configuration Management Plan for the NWC SAF	NWC/CDOP3/SAF/AEMET/MGT/CMP	1.1	15/04/20
[AD.4]	System and Components Requirements Document for the NWC/GEO	NWC/CDOP3/GEO/AEMET/SW/SCRD	1.0	01/09/21
[AD.5]	Interface Control Document for Internal and External Interfaces of the NWC/GEO	NWC/CDOP3/GEO/AEMET/SW/ICD/1	2.0	01/09/21
[AD.6]	Interface Control Document for the NWCLIB of the NWC/GEO	NWC/CDOP3/GEO/AEMET/SW/ICD/2	2.0	01/09/21
[AD.7]	Data Output Format for the NWC/GEO	NWC/CDOP3/GEO/AEMET/SW/DOF	2.0	10/01/22
[AD.8]	Component Design Document for the NWCLIB of the NWC/GEO	NWC/CDOP2/GEO/AEMET/SW/ACDD/NWCLIB	2.0.1	31/07/18
[AD.9]	NWC SAF Product Requirements Document	NWC/CDOP3/GEO/AEMET/MGT/PRD	1.5	01/12/21
[AD.10]	User Manual for the Tools of the NWC/GEO	NWC/CDOP3/GEO/AEMET/SCI/UM/Tools	2.0	10/01/22

Table 1: List of Applicable Documents

1.5.2 Reference Documents

The reference documents contain useful information related to the subject of the project. This reference document complements the applicable documents. For dated references, subsequent amendments to, or revisions of, any of these publications do not apply. For undated references, the latest edition of the document referred to applies.

Latest documentation can be found at the NWC SAF Help Desk at http://www.nwc-saf.eumetsat.int

Reference	Title	Code	Version	Date
[RD.1]	The Nowcasting SAF Glossary	NWC/CDOP3/SAF/AEMET/MGT/GLO	1.0	20/10/20
[RD.2]	Product User Manual for the "Automatic Satellite Image Interpretation" product (ASII, PGE10)	SAF/NWC/CDOP2/ZAMG/SCI/PUM/10	2.4.2	15/07/13
[RD.3]	Scientific and Validation Report for the "Automatic Satellite Image Interpretation – Next Generation" Processors of the NWC/GEO	NWC/CDOP3/GEO/ZAMG/SCI/VR/ASII-NG	1.0	21/01/19
[RD.4]	Scientific and Validation Report for the "Automatic Satellite Image Interpretation – Next Generation" Processors of the NWC/GEO	NWC/CDOP3/GEO/ZAMG/SCI/VR/ASII-NG	2.0	10/01/22

Table 2: List of Referenced Documents

2. AREAS WITH RISK OF CAT – OVERVIEW

During the precedent phases of NWCSAF, the Automatic Satellite Image Interpretation (ASII) product has been developed to analyse satellite imagery in terms of conceptual models of atmospheric phenomena, e.g. cold fronts, warm fronts, dry intrusions, etc. It came to a point that the conceptual model method could no longer be improved, and so it was decided in the "Next-Generation" (NG) product to employ new methods of analysis to detect selected features in satellite data. These features, having the importance to aviation in common, will be discussed in some detail in the following sections.

Clear-air turbulence is the turbulent movement of air masses in the absence of any visual clues such as clouds outside the planetary boundary layer, often in the upper troposphere. CAT typically has a patchy structure and horizontal dimensions of 80-500 km in the along-wind direction and 20-100 km in the across-wind direction. Vertical dimensions are 500-1000 m, and the lifespan of CAT is between half an hour and a day (Overeem, 2002). Forecasts of CAT in numerical weather models are difficult to perform because the scale of the physical processes involved in turbulence are smaller than most model resolutions. Thus it is of interest here to develop a method to at least identify areas from satellite data which show (high) risks of CAT.

As its name suggests, CAT cannot be observed directly from satellite imagery since it occurs in cloud free regions. However, there exist several indicators in the vicinity of a region of CAT which can be observed in satellite data which provide an indication that CAT is likely to occur.

3. ALGORITHM DESCRIPTION

3.1 THEORETICAL DESCRIPTION

3.1.1 Physics of the problem

The role of ASII-NG is to detect regions of turbulence based on meteorological parameters and combinations thereof that are indicators of turbulence.

In general, CAT occurs preferentially in the following meteorological situations:

- Tropopause folds
- Gravity waves (e.g. lee waves)
- Air mass boundaries (e.g. fronts)
- Wind shear (e.g. jets)
- Convection

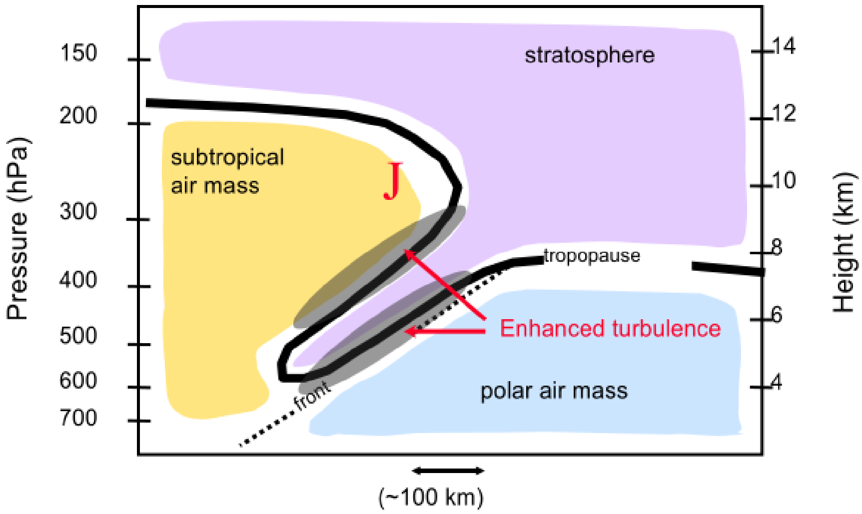

Figure 1: Schematic of a tropopause fold[1].

A tropopause fold describes the downward intrusion of stratospheric air into the troposphere which results in a "folding" of the tropopause, as schematically illustrated in Figure 1. Typically, at a tropopause fold there is the vertical shearing at the jet stream combined with the ageostrophic convergence of polar, subtropical, and stratospheric air masses. Tropopause folds mark the change in the height of the tropopause and are characterized by the occurrence of strong turbulence. Stratospheric air, which characteristically has a low moisture content and a high potential vorticity can protrude down to the mid or even the lower troposphere. Consequently, tropopause folds can be located by their association with gradients in upper level moisture, which are evident in the SEVIRI 6.2 µm channel sensitive to upper tropospheric water vapour. A tropopause folding turbulence product based on the ABI (Advanced Baseline Imager) sensor flown on the GOES-R series of NOAA geostationary meteorological satellites and using the 6.1 µm channel has been developed by NOAA NESDIS (Wimmers and Feltz, 2010). The tropopause height can be

[1] Schematic courtesy of Feltz and Wimmers, 2010: "GOES-R AWG Aviation Team: Tropopause Folding Turbulence Prediction (TFTP)"

determined from NWP parameters such as the temperature, specific humidity or potential vorticity. The ozone content derived from SEVIRI IR channel at 9.7 µm is a good indicator for the presence of a tropopause fold. The lower the tropopause the more ozone is sensed by the SEVIRI instrument onboard MSG satellites. Air mass boundaries, which often coincide with tropopause folds, can be determined from satellite data. Transition zones between polar and tropical air masses are reflected in the MSG "ozone channel" IR 9.7 µm.

In the lee of mountain ridges, turbulence occurs below lee waves where a rotor cloud can develop. The turbulence cannot be directly seen, but mountain waves show the typical pattern of parallel white lines aligned perpendicular to the wind direction. Two kinds of lee waves can be discriminated: trapped lee waves which are bound to a certain layer (due to stratification they cannot propagate across an "upper" and a "lower" border) and non-trapped lee waves which are propagating both in vertical and horizontal directions. The energy balance is different for those two cases. For the trapped lee waves the energy of the waves is conserved within the layer – with an exchange of energy from non-turbulent to turbulent flow, whereas in the latter case energy can be transported vertically.

One criterion to estimate turbulence is the existence of a foehn gap between mountain ridge and lee clouds (Ellrod and Knox, 2010). In the case of turbulence, a pronounced sinking zone can be seen in WV, VIS and IR images. There also exists a correlation between wave length and turbulence intensity. In addition, the intensity of turbulence may be assessed by the complexity of the cloud pattern; the more complex the pattern is (e.g. crossing wave fronts) then the higher the intensity of turbulence (Uhlenbrock et al., 2007). However, these factors can probably be applied only to a very limited extent in an automatic detection tool.

Although lee clouds can be expected behind large surface elevations like mountain ranges or elevated coasts, they can also occur in lee of small hills or islands. Important for the formation of lee waves is the angle between the main wind direction and the orientation of the mountain range, and the stability of the layer of air. Ideal conditions for the appearance of lee waves occur when the air flow is near to perpendicular to the surface elevation. The wind speed ideally should exceed a certain value to allow the air flow to overflow the mountain range rather than to circulate around. In case of mountain heights up to 1000 m the wind speed should be larger than 8-10 m/s, while for higher mountain ranges, a wind speed of more than 12-15 m/s is necessary (World Meteorological Organization, 1978). An increase of the wind speed up to 20-25 m/s has shown beneficial for the development of lee waves. Lee wave development ideally occurs when the wind direction is constant with height, although variations up to 20°/ 1000m do not affect their development.

At the edge of polar fronts and in the cirrus plume associated with subtropical jets, transverse cloud bands can sometimes be observed in the IR satellite images. Turbulence at jet level originates from large vertical wind shear (Bader et al. 1995). Friction among layers with varying wind speed leads to the formation of small scale eddies (Kelvin-Helmholtz instability). Transversal cloud bands are a good indicator of turbulence at jet level.

In cases where a thermal inversion separates two layers with a marked difference in wind direction and/or speed (i.e. wind shear), gravity waves may be produced. If the wind encounters distortions at the inversion layer caused by thermals coming up from below, it will create significant shear waves in the lee of the distortions.

Turbulence is closely related to convection. Vertical mass exchanges lead to up- and downdrafts causing turbulence. However, ASII-NG intentionally does not deal with the detection of convective cells as this topic is covered elsewhere in the NWCSAF portfolio, namely in the RDT-CW product.

Algorithms developed previously to predict/analyse the occurrence of CAT were primarily based on NWP output (Elrod and Knapp, 1991), not taking into account information provided by satellite sensors. A typical example for a turbulence warning system is the Graphical Turbulence Guidance (GTG and GTG2), developed by NCAR (Sharman et al., 2004). There currently exist a large number of numerical parameters to diagnose turbulence, but to date an all-encompassing parameter does not exist. For example, potential vorticity is critical to the detection of tropopause folds (Wimmers and Feltz, 2010); PVA is considered to be the leading parameter in the detection of gravity waves associated with jets (transverse bandings; Knox et al., 2007); vorticity and upper level divergence are considered relevant for transverse bandings at the outflow of thunderstorms (Lenz, 2008). When considering mountain waves, characteristic numbers describing the flow, and layer stability, e.g. the Richardson Number (McCann, 2001), or some special indices developed for classifying turbulence (Ellrod Index, Brown Index, Dutton Index) are the most important measures of turbulence (Overeem, 2002). When using NWP data, the resolution of the model is crucial since turbulence is a small-scale phenomenon and is not resolved by common operational models.

3.1.2 Mathematical description of the algorithm

3.1.2.1 Logistic regression

Ideally, the outcome of a subjective image interpretation with respect to a certain phenomenon is a binomial one, segregating the image into areas of "present" (=1) and "not present" (=0). The parameters used to arrive at that conclusion are typically continuous. A logistic regression is a possible framework to formalize that situation in a mathematical model required to attempt automatic image interpretation. As in an ordinary multiple regression, we have a dependent variable Y and several independent variables X_i tied together in a linear combination. However, the governing equation in logistic regression is somewhat more complex in order to account for the dichotomous nature of the predictand Y (P is the probability that Y=1):

$$\ln[P/(1-P)]=b_0+b_1X_1+b_2X_2+b_3X_3...$$

In order to establish the regression relation for ASII-TF, test samples had to be collected. A sample size of 30 scenes was used, where the tropopause defined by 2 PVU (potential vorticity units)-surfaces of ECMWF analyses helped to pick pixels from the two categories 1) likely at a tropopause fold and 2) certainly not at a tropopause fold. Providing these diagnoses and the predictands X_i for the respective (almost 1.5 million) pixels, regression coefficients b_i can be deduced through an iterative computation. Once this is achieved, the rest (i.e. the actual derivation of the product) is straightforward: Assemble the input data for the requested slot, compute the variables X_i and derive the probability for the presence of the phenomenon at every pixel (with the above equation solved for P).

3.1.2.2 ASII-TF

Table 3 shows the input parameters required for the detection of turbulence related to **tropopause folds**. Based on specific humidity, one height of the tropopause [hPa] is calculated from the NWP data. It is the gradient field that serves as input into the logistic regression. It is recommended that NWP data be provided up to the 50 hPa level to ensure that the tropopause is captured (on the other hand, it was found for the GFS model that the humidity fields in layers above 30 hPa are not dependable. Random fluctuations with often unrealistic increases at high levels accidentally satisfy the tropopause criteria. In order to avoid such erroneous signals, the ASII-TF software simply omits NWP input from layers with <30hPa pressure, as the tropopause should be located in lower layers anyway).

Brightness temperatures from channels WV 6.2 µm directly serve as input, yet there are also some post-processed satellite data involved: From WV 6.2, also the gradient is input; moreover, the dark-stripe detection described in Jann (2002) is applied to a somewhat smoothed version of the field, and it is the distance from the stripe edge that serves as one of the predictors. The channel difference IR 9.7 µm – IR 10.8 µm enters the logistic regression relation in form of its gradient field.

NWP parameter	Satellite data
specific humidity	WV 6.2 µm
wind speed at 300 hPa	IR 9.7 µm
absolute value of shear vorticity at 300 hPa	IR 10.8 µm

Table 3: Input parameters from NWP and satellite data for the detection of tropopause folds

3.1.2.3 ASII-GW

For the detection of mountain waves and transversal bandings, a method had to be implemented which can detect parallel cloud bands on meso-gamma (2-20 km) to meso-beta (20-200 km) range. The difference between the two meteorological phenomena is the circumstance that transverse banding occurs at the edge of (frontal) cloud bands at jet level while mountain waves typically appear in the low to mid troposphere and are independent of other cloud features. However, there are situations where mountain waves are embedded within fronts. In any case, the phenomena are reflected in the satellite imagery by patterns of parallel dark and white stripes in alternation. For detecting them objectively, an approach advocated in a series of papers by a pair of authors (Kruizinga and Petkov, 1995, 1999; Petkov and Kruizinga, 1997) was adopted. They employed Gabor filters to identify single stripes, and subsequently applied so-called grating cell operators which looked for configurations of three stripes in equal distance. In our application, we apply the approach to the WV 7.3 and IR 10.8 channels. They can yield complementary signals, e.g. a strong argument in favour of using WV 7.3 is given by Feltz et al. (2009): the results of the vertical motions induced by gravity waves may be seen there even if the atmospheric conditions are not favourable enough for the development of clouds which is the prerequisite for identifying the gravity waves in visible and infrared bands.

The Kruizinga-Petkov model is based on Gabor filter functions $g(x, y)$ described as follows:

$$g_{\xi,\eta,\lambda,\Theta,\varphi}(x,y) = exp\left(-\frac{x'^2+\gamma^2 y'^2}{2\sigma^2}\right) cos\left(2\pi\frac{x'}{\lambda}+\varphi\right), \quad [1]$$

$$x' = (x-\xi)cos\Theta + (y-\eta)sin\Theta, \quad [2]$$

$$y' = -(x-\xi)sin\Theta + (y-\eta)cos\Theta, \quad [3]$$

where the parameters have the following meaning:

(ξ, η) are the coordinates of the filter centre, (x, y) are those of the pixels in the surrounding. The standard deviation σ of the Gaussian factor determines the size of the field considered around (ξ, η) (cf. parameter Ω in the following Eq. 4). The eccentricity of the filter is steered by the spatial aspect ratio γ. The parameter λ, which is the wavelength of the cosine factor, will eventually correspond to the spatial frequency of the periodic patterns detected best. The parameter $\Theta \in [0, \pi)$ specifies the orientation of the normal to the parallel stripe zones (this normal is the axis x' of Eq. 2). Finally φ, the phase offset in the argument of the harmonic factor, determines the symmetry of the function. However, only symmetric filters with φ=0 and φ=π, respectively, will actually be used in the following. It helps in building an efficient numerical implementation to note that with a phase shift of π, the Gabor function values differ only in their signs, i.e. $g_{\xi,\eta,\lambda,\Theta,\varphi=\pi}(x,y) = -g_{\xi,\eta,\lambda,\Theta,\varphi=0}(x,y)$. Figure 2 offers graphical sketches of two Gabor filter matrices.

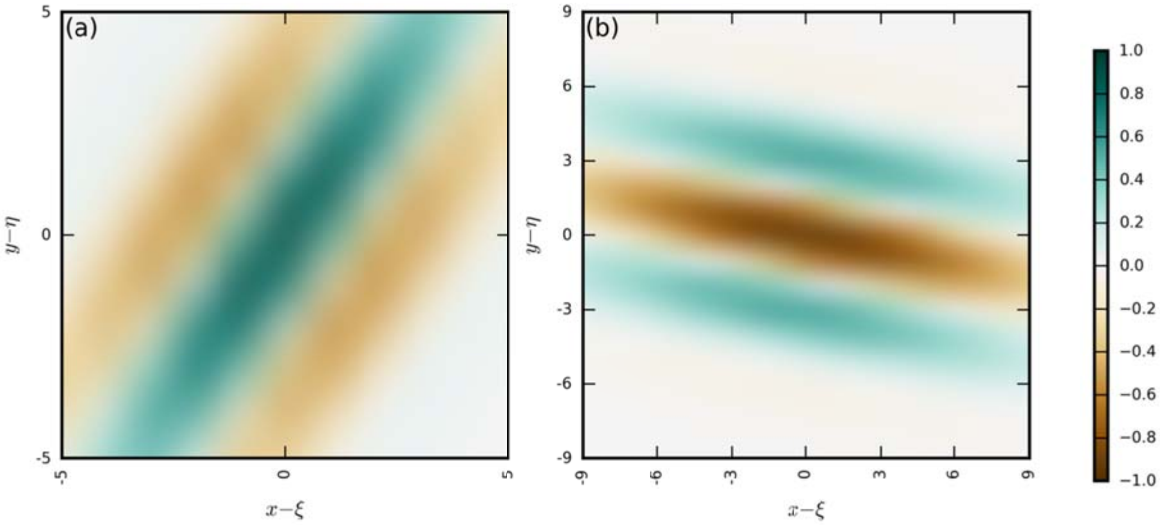

Figure 2: Graphical representation of two Gabor filter functions used in the gravity wave detection. (a) γ=0.4, σ=2.0, λ=5, Θ=13π/16, φ=0, (b) γ=0.4, σ=2.8, λ=7, Θ=7π/16, φ=π.

The filter response at any location (ξ, η) is obtained by convolving $g(x, y)$ with the WV7.3 brightness temperature image $f(x, y)$ in a vicinity Ω around (ξ, η):

$$r_{\xi,\eta,\lambda,\Theta,\varphi} = \iint_{\Omega} f(x, y)\; g_{\xi,\eta,\lambda,\Theta,\varphi}(x, y) dx\, dy. \quad [4]$$

In order to make the results invariant against addition of a constant value to the input image, additional measures have to be taken. The approach discussed in Lourens (1998) was adopted where all negative values resulting from Eq. 1 are multiplied by a factor, which is obtained by summing the positive values of Eq. 1 and dividing the sum by the negative sum of the negative values. In order to preserve invariance against the sign of the image input (this symmetry is indispensable as the notion of "bright" and "dark" in imagery outside the visible spectrum is just a matter of convention), this modification of negative filter coefficients is done only for φ=0. The relation $g_{\xi,\eta,\lambda,\Theta,\varphi=\pi}(x, y) = -g_{\xi,\eta,\lambda,\Theta,\varphi=0}(x, y)$ remains in force and provides the Gabor function values for $\varphi = \pi$.

The values $r_{\xi,\eta,\lambda,\Theta,\varphi}$ are withheld from further processing when falling below a threshold r_{min} (in other words, demanding a certain minimum response). For setting the threshold r_{min}, the convolution of the Gabor filter with an amplitude-adjusted copy of itself was computed, with the idea behind that the signal from a perfectly matching pattern with very small magnitude is assessed. This threshold magnitude is set to 0.17 K brightness temperature for MSG WV7.3 and 1.5 K for MSG IR10.8 (0.3 and 2.2 K, respectively for the corresponding channels on MTG/Himawari/GOES-R with higher spatial resolutions and resulting sharper contrasts). In the WV analysis branch, we moreover set $r_{\xi,\eta,\lambda,\Theta,\varphi}$=0 for pixels with WV7.3 brightness temperature below -30°C, which effectively eliminates spurious, comparatively erratic, signals from randomly matching minor water vapour fluctuations in thick cloud decks (see Jann, 2017, for more details).

After having obtained $r_{\xi,\eta,\lambda,\Theta,\varphi}$ for all (ξ, η), the subsequently applied grating cell operator inspects along a straight line, direction prescribed through the angle Θ, the values orthogonal to the orientation of the filter's bars. A quantity $q_{\xi,\eta,\Theta,\lambda}$, is determined at all (ξ, η):

$$q_{\xi,\eta,\Theta,\lambda} = \begin{cases} 1, if\ \forall n, M_{\xi,\eta,\lambda,\Theta,n} \geq \rho m_{\xi,\eta,\lambda,\Theta} \\ \\ 0, if\ \exists n, M_{\xi,\eta,\lambda,\Theta,n} < \rho m_{\xi,\eta,\lambda,\Theta}, \end{cases} \qquad [5]$$

where $n \in \{-n_{max}, \dots, n_{max}\}$ (n_{max} thus defining how many adjacent stripes one wishes to find), ρ is "a threshold parameter with a value smaller than but near one" (Kruizinga and Petkov, 1995) and the auxiliary quantities $m_{\xi,\eta,\lambda,\Theta}$ and $M_{\xi,\eta,\lambda,\Theta,n}$ are computed as follows:

$$M_{\xi,\eta,\lambda,\Theta,n} = max\{r_{\xi',\eta',\lambda,\Theta,\varphi_n} | \xi', \eta':$$

$$\left\lfloor n\frac{\lambda}{2\cos\psi}\cos(\Theta+\psi)\right\rfloor \leq (\xi' - \xi) \leq \left\lceil n\frac{\lambda}{2\cos\psi}cos(\Theta+\psi)\right\rceil, \qquad [6]$$

$$\left\lfloor n\frac{\lambda}{2\cos\psi}sin(\Theta+\psi)\right\rfloor \leq (\eta' - \eta) \leq \left\lceil n\frac{\lambda}{2\cos\psi}sin(\Theta+\psi)\right\rceil\};$$

$$m_{\xi,\eta,\lambda,\Theta} = max\{M_{\xi,\eta,\lambda,\Theta,n} | n = -n_{max}, \dots, n_{max}\} \qquad [7]$$

with $\lfloor x \rfloor$ representing the floor operator (nearest integer value smaller than or equal to *x*) and $\lceil x \rceil$ designating the ceiling operator (nearest integer value larger than or equal to *x*). It is irrelevant whether the pixel at the center of the grating pattern is dark or bright. Therefore: (1) in case $r_{\xi,\eta,\lambda,\Theta,\varphi=0}$ is larger than the threshold r_{min}, the test is run with $\varphi_n = 0$ for even n and $\varphi_n = \pi$ for the uneven n; (2) if r_{min} is exceeded for $r_{\xi,\eta,\lambda,\Theta,\varphi=\pi}$, the test is run with $\varphi_n = \pi$ for the even n and $\varphi_n = 0$ for the uneven values. ψ indicates that the search takes place not only orthogonal to the filter's bars; the set of deflections used is: -30°, -20°, …, 0, …20°, 30°. Figure 3 translates formulas [6] and [7], describing the search algorithm, into a graphical representation. 8 values of Θ are used, namely π/16, 3π/16, …, 15π/16; gravity waves exhibit an anisotropic appearance, i.e. a regularity of lines, over a larger area whereas marine stratocumulus (a potential source of false alarms in ASII-GW) are characterised over most parts by a regularity of patches. For many pixels in a Stratocumulus area, there are alternating white and black signals in a certain direction but comparably so in other, perhaps even perpendicular, directions. Consequentially, the idea is to separate the anisotropic from the isotropic cases through comparing the eight Gabor filter responses obtained for the eight values of Θ at (ξ, η) for a given λ, and to retain at every pixel only the $r_{\xi,\eta,\lambda,\Theta,\varphi}$ with the highest absolute value before we enter the tests [5]-[7].

The test returns a hit, signaling a grating pattern, if alternating Gabor filter signals of the same preferred orientation Θ and spatial frequency $1/\lambda$ have similar magnitudes in intervals of length $\lambda/(2\cos\psi)$ along a line passing in direction $\Theta + \psi$, having length $n_{max}\lambda/\cos\psi$ and being centered on point (ξ, η). It is of course unrealistic to expect that all stripes in a satellite image look the same. Therefore, a certain tolerance is introduced into the above formulas, via parameter ρ.

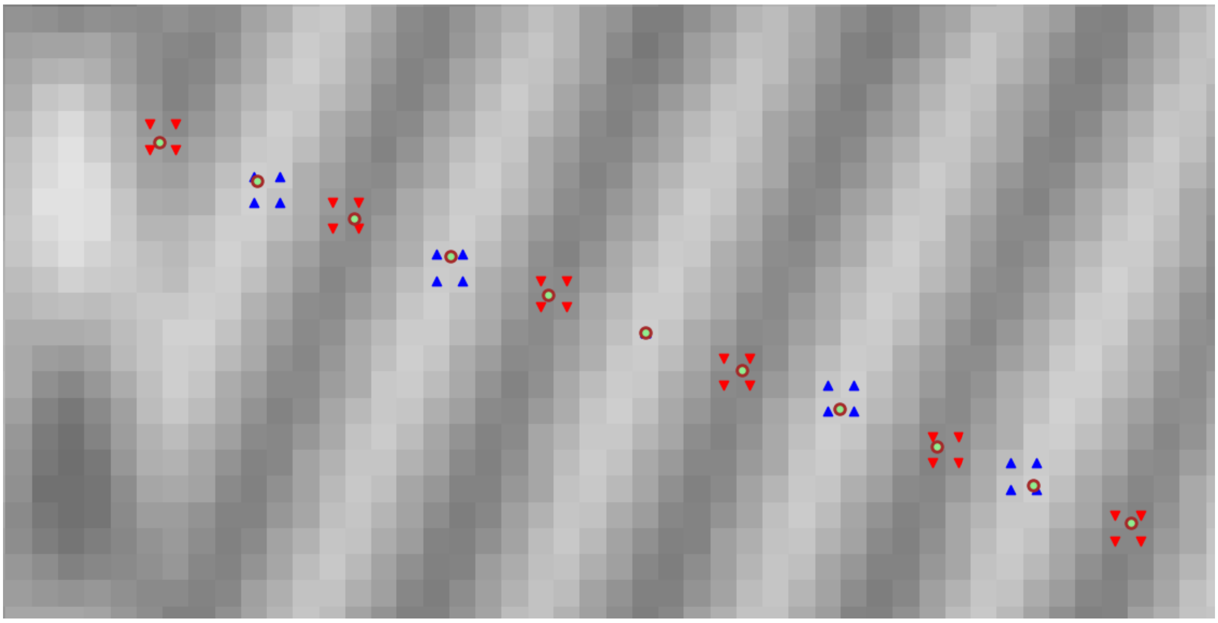

Figure 3: Schematic of the grating detection. In principle, the situation is evaluated at the dots in equidistant spacing, but as one often lies at the edge of pixels, a tolerance is applied and the four closest pixels are examined. As the pixel at the centre of the search line has a Gabor value typical for a white stripe, the pixels marked with the blue triangles are checked for being characteristic for white stripes, whereas at least one in each red-triangle group should show a strong dark-stripe signal.

In order to transform the signals $q_{\xi,\eta,\Theta,\lambda}$=1 into the required "probability of gravity wave" field, one could use a distance-weighted spatial integration (similar to what was suggested in Kruizinga and Petkov (1999):

$$w_{\xi,\eta,\Theta,\lambda} = \iint_{\Omega_w} \exp\left(-\frac{(\xi-\xi')^2+(\eta-\eta')^2}{2\sigma_w{}^2}\right) q'_{\xi',\eta',\Theta,\lambda}(x,y)d\xi'd\eta' \quad [8]$$

Integration area and standard deviation of this filter are unrelated to Eqs. 1 and 4, and in fact differ, hence the subscript w appears on Ω and σ. The motivation of introducing a new parameter q' is as follows: The q of Eq. 5, taken from the original Kruizinga-Petkov formulation, assumes 1 only for the central point of the line along which a grating pattern is detected. Yet, one can exploit the available information about extension and orientation of the phenomenon by distributing the numerical contribution of 1 evenly over that line. Therefore, $1/L$ is added to the array q' at all L pixels along the search line (as determined from the two end points through Bresenham's (1965) line algorithm). Thus, every instance of q=1 equally contributes a total of 1 regardless of λ, and the results for the different wavelengths remain comparable. This is important since the computation of $w_{\xi,\eta,\Theta,\lambda}$ is done separately for each tested combination of Θ and λ, and the maximum density observed for any single Θ-λ pair constitutes the final output at (ξ,η). This proceeding favours regions where numerous signals are found for one specific parameter setting.

Next, the resulting maximum-density function $w_{\xi,\eta}$ is projected with a logistic function onto the (0%, 100%) range. One may regard this as a limit case of logistic regression where only one predictor variable is used. Should a future validation campaign reveal a benefit of additional predictors, they can easily be combined with the $w_{\xi,\eta}$ in the full regression framework indicated above.

It remains to list the parameter setting on which we finally settled for vMTG-I day-1, after four years of working with the algorithm: γ=0.4; $n_{max} = 5$; $\rho = 0.1$; 12 values of λ, namely 2, 2.5…,7, 7.5 image pixels; $\sigma = 0.4 * \lambda$; σ_w=5 pixels and Ω_w is a 31×31-pixels square. For geometrical reasons, gravity waves near the edge of the disc are not resolved by a geostationary satellite; even worse, false alarms were observed there, where pixels with very large mutual distances (in metric terms) were accidentally exhibiting regularities. Hence, an upper limit on the actually tested values of λ was introduced (a cosine function of the satellite zenith angle that assumes the value of 2 at pixels (ξ, η) with 60° zenith angle, i.e. for pixels viewed even more slantwise, no detection attempt is actually made).

Note that the evolution of the algorithm and the motivation behind some of the settings is documented in the two papers of Jann (2017, 2019), and the description here is just a technical summary of the essential algorithmic parts.

3.2 PRACTICAL CONSIDERATIONS

3.2.1 Validation

ASII-NG uses predefined criteria to detect regions favourable for turbulence, based primarily on satellite data. The absence of these criteria in the data does not automatically mean the absence of turbulence, since not all mechanisms of turbulence can be captured by ASII-NG (see also section 4). Thus it is not a fair measure of ASII-NG's performance to compare its detected "fields prone to turbulence" with actual fields of turbulence, since ASII-NG can only detect a subset of all turbulent fields. Validation of ASII-NG will therefore place more emphasis on the analysis of the structures detected. This means that validation will be (at least partly) subjective by checking if the indication of a certain pattern (which is commonly accepted as related to turbulence) would be agreed by a meteorologist, too.

A verification of turbulence itself is very problematic. PIREPS (=pilot reports) could be used to check that areas recognized as being favourable for turbulence by ASII-NG were indeed found to be accompanied by turbulence. The problems with that method are, however, that PIREPS just provide reports when turbulence is present, with decision on issuance taken subjectively (although there are airplanes with instruments measuring vertical acceleration). Furthermore, the reports are bound to flight routes, thus unevenly distributed and in regions without air traffic no verification can be obtained at all. For a more comprehensive reading about difficulties of verification against PIREPs, the interested reader may like to consult the paper of Brown and Young (2000).

The approaches followed by the evaluators in this situation were somewhat different for the two sub-products; see the validation reports [RD.3], [RD.4] for details.

3.2.2 Quality control and diagnostics

In its current version, ASII-TF cannot provide results at pixels for which one (or more) required input parameters are unavailable. The information regarding which input parameter(s) was/were missing is included as a separate flag field in the ASII-TF output file (field "asii_turb_trop_prob_status_flag"; cf. its more detailed description in ch. 3.2.3).

ASII-GW features analyses based on WV7.3-only and/or IR10.8(10.5)-only as input, and can of course not provide a result for any invalid pixel in the respective channel. At the edges of the analysed image, vicinity evaluations as in Eqs. 6 and 8 are not possible for all Θ-λ pairs; the code for "questionable" is assigned to the affected pixels in the asiigw_quality flag in order to distinguish them from the pixels where the full test battery could be run.

3.2.3 Description of the output

The ASII-NG products are encoded in standard NWCSAF netCDF output files. As such, they feature many standard entries/matrices common to all NWC/GEO netCDF products; such contents are described in the NWCSAF Data Output Format Document [AD.7]. There is one file per slot per sub-product, and the output files are located by default in $SAFNWC/export/ASII; the naming follows the schematic S_NWC_ASII-<*sub-product*>_MSG*i*_<*region*>-VISIR_*YYYYMMDD*T*hhmmss*Z.nc (examples: S_NWC_ASII-GW_MSG3_global-VISIR_20150626T120000Z.nc and S_NWC_ASII-TF_MSG3_global-VISIR_20150626T120000Z.nc).

Apart from the standard fields, the netCDF file holds the following ASII-NG-specific fields:

- (ASII-TF) "asiitf_prob": derived probability for occurrence of tropopause folding; for each pixel a value between 0 and 100%, with failure to derive it at a certain pixel indicated by code 255.
- (ASII-TF) "asiitf_status_flag": giving more details on reasons why "asiitf_prob" could not be derived at a certain pixel. 0=everything OK, probability computed; otherwise:
    - bit 1 set: problem in "stripe in WV6.2"
    - bit 2 set: problem in "(gradient in) WV6.2"
    - bit 3 set: problem in "gradient of the difference image IR9.7-IR10.8"
    - bit 4 set: problem in "shear vorticity" (NWP parameter)
    - bit 5 set: problem in "wind speed" (NWP parameter)
    - bit 6 set: problem in "tropopause from specific humidity" (NWP parameter that may require model levels in great height)
- (ASII-GW) asiigw_ir_prob_pal, asiigw_wv_prob_pal; (ASII-TF) asiitf_prob_pal: turquoise (0)-to-red (100%) palettes
- (ASII-GW) "asiigw_wv_prob", "asiigw_ir_prob": derived probability for presence of gravity wave in the WV and IR channel, respectively; for each pixel a value between 0 and 100%, with failure to derive it at a certain pixel indicated by code 255.
- (ASII-GW) "asiigw_status_flag": giving more details on reasons why "asii_turb_wave_prob" could not be derived at a certain pixel. 0=everything OK, probability computed; otherwise:
    - bit 1 set: not a valid WV7.3 pixel
    - bit 2 set: pixel filtered by temperature threshold in WV7.3
    - bit 3 set: not a valid IR10.8/10.5/11.2 pixel
    - bit 4 set: pixel filtered by temperature threshold in IR10.8/10.5/11.2
- (ASII-GW) "asiigw_wv_continuity", "asiigw_ir_continuity": indicating the number of slots a gravity wave probability > 0% has been obtained at the pixel in the WV and IR channel, respectively, without interruption (currently testing up to 7 preceding analyses in $SAFNWC/export/ASII; i.e. 8 being the maximum number, 1 meaning that it appeared for the first time in the current analysis).
- the common processing conditions and quality flags (described in [AD.7]) for these products bear the names asiigw_conditions/asiitf_conditions and asiigw_quality/asiitf_quality.

4. ASSUMPTIONS AND LIMITATIONS

These products are aimed to be part of the inputs for decision making by meteorologists, yet cannot be used as a stand-alone automatic warning tool. The products are satellite products searching for features favourable for turbulence but NOT the turbulence itself. As CAT by definition is a clear-air phenomenon there may be areas of turbulence which cannot be detected by any remote sensing tool. Therefore, the absence of signals in satellite imagery does not preclude the presence of CAT. In other words, even assuming the detection algorithms are working perfectly, the detection rate of CAT will never reach 1.

Although the NWCSAF software package can be processed at any region of the disc, the focus of tuning and validation was on Europe and the neighbouring sea areas (although the validation exercise for ASII-GW v1.0 included visits to areas on the whole disc including the southern hemisphere [RD.3]; Jann (2019)). The higher resolution of Himawari/GOES-R/MTG-FCI means that gravity waves with smaller wavelengths can be inspected. Given the typical scale of tropospheric gravity waves, this should have a positive impact on detectability. Still, for geometrical reasons, one must accept that gravity waves near the edge of the disc are not resolved or, in general terms, that the detection rate has an irremediable dependence on the satellite zenith angle.

5. REFERENCES

Bader, M.J., Forbes, G.S., Grant, J.R., Lilley, R.B.E., and A.J. Waters (Eds.), 1995: Images in weather forecasting. Cambridge University Press, Cambridge.

Bresenham, J.E., 1965. Algorithm for computer control of a digital plotter. IBM Systems Journal **4,** 25-30.

Brown, B.G., and G.S. Young, 2000: Verification of icing and turbulence forecasts: Why some verification statistics can't be computed using PIREPS. 9th Conference on Aviation, Range, and Aerospace Meteorology, Orlando, FL, 11-15 September 2000, 393-398.

Ellrod, G.P., and D.J. Knapp, 1991: An Objective Clear-Air Forecasting Technique: Verification and Operational Use, Weather and Forecasting, **7,** 150-165.

Ellrod, G.P., and J.A. Knox, 2010: Improvements to an Operational Clear-Air Turbulence Diagnostic Index by Addition of a Divergence Trend Term, Weather and Forecasting, **25,** 789–798. doi: http://dx.doi.org/10.1175/2009WAF2222290.1

Feltz W.F., Bedka K.M., Otkin J.A., Greenwald T., and S.A. Ackerman, 2009: Understanding satellite-observed mountain-wave signatures using high-resolution numerical model data. Weather and Forecasting, **24,** 76-86. doi: 10.1175/2008WAF2222127.1.

Jann, A., 2002: Use of a simple pattern recognition approach for the detection of ridge lines and stripes. Meteorological Applications, **9,** 357-365.

Jann A., 2017: Detection of gravity waves in Meteosat imagery by grating cell operators. European Journal of Remote Sensing, **50,** 509-516.

Jann, A., 2019: Objective detection of stripe patterns in satellite imagery caused by gravity waves: Lessons learnt from the southern hemisphere. Transactions of the Royal Society of South Africa, **74,** 163-172, https://doi.org/10.1080/0035919X.2019.1596176.

Knox, J.A., McCann, D.W., and P.D. Williams, 2007: Application of the Lighthill–Ford Theory of Spontaneous Imbalance to Clear-Air Turbulence Forecasting, Journal of the Atmospheric Sciences, **65,** 3292–3304.

Kruizinga, P., and N. Petkov, 1995: A computational model of periodic-pattern-selective cells. In: Mira J., Sandoval F. (Eds.), Proc. IWANN'95, Lecture Notes in Computer Science 930, Springer, pp. 90–99.

Kruizinga, P., and N. Petkov, 1999: Nonlinear operator for oriented texture. IEEE Transactions on Image Processing, **8,** 1395-1407. doi: 10.1109/83.791965.

Lenz, A., 2008: Identification of Transverse Band Signature in Satellite Imagery, http://www.nwas.org/committees/rs/2008_MetSat_Papers/Lenz.pdf

Lourens, T. ,1998: A biologically plausible model for corner-based object recognition from color images. Shaker Publishing B.V., Maastricht.

McCann, D., 2001: Gravity Waves, Unbalanced Flow and Aircraft Clear Air Turbulence, National Weather Digest, **25,** 3-14.

Overeem, A., 2002: Verification of clear-air turbulence forecasts, Technisch rapport; TR-244, KNMI, De Bilt.

Petkov, N., and P. Kruizinga, 1997: Computational models of visual neurons specialised in the detection of periodic and aperiodic oriented visual stimuli: bar and grating cells. Biological Cybernetics, **76,** 83-96.

Sharman, R., Tebaldi, C., Wiener, G., and J. Wolff, 2006: An Integrated Approach to Mid- and Upper-Level Turbulence Forecasting, Weather and Forecasting, **21,** 268-287.

Uhlenbrock, N.L., Bedka, K.M., Feltz, W.F., and S.A. Ackerman, 2007: Mountain Wave Signatures in MODIS 6.7µm Imagery and Their Relation to Pilot Reports of Turbulence, Weather and Forecasting, **22,** 662-670.

Wimmers, A., and W. Feltz, 2010: Tropopause Folding Turbulence Product, Algorithm Theoretical Basis Document, UW/CIMSS, Version 2.0, May10, 2010. (http://www.goes-r.gov/products/ATBDs/option2/Aviation_Turbulence_v1.0_no_color.pdf).

World Meteorological Organization, 1978: Handbook of Meteorological Forecasting for Soaring Flights, WMO Technical Note Nr. 158.

ANNEX 1: ANCILLARY DATA

The ASII-TF sub-product of ASII-NG v2.1 makes use of the NWP fields of temperature, humidity and wind on all pressure levels listed in the central NWP configuration file (if available in the local GRIB file)